



## Research paper

# Cogeneration of ethylene and energy in protonic fuel cell with an efficient and stable anode anchored with *in-situ* exsolved functional metal nanoparticles

Subiao Liu<sup>a</sup>, Qingxia Liu<sup>a</sup>, Xian-Zhu Fu<sup>b,\*</sup>, Jing-Li Luo<sup>a,\*</sup><sup>a</sup> Department of Chemical and Materials Engineering, University of Alberta, Edmonton, Alberta T6G 1H9, Canada<sup>b</sup> College of Materials Science and Engineering, Shenzhen University, Shenzhen 518060, China

## ARTICLE INFO

## Keywords:

Protonic fuel cell  
Ethane dehydrogenation  
*in situ* exsolution  
Metal nanoparticle  
Anode catalyst

## ABSTRACT

*In situ* exsolution of Co nanoparticles on perovskite framework has been successfully synthesized by firing the porous precursor  $\text{SrMo}_{0.8}\text{Co}_{0.1}\text{Fe}_{0.1}\text{O}_{3-\delta}$  (SMCFO) in reducing flow at 850 °C. A structure transformation (from mixed to pure cubic phase) and the growth of Co nanoparticles are observed in  $\text{H}_2$  atmosphere. This leads to an increase in the oxygen vacancy content, which is beneficial to the electrical conduction and catalytic activity towards the oxidations of  $\text{H}_2$  and  $\text{C}_2\text{H}_6$ . Moreover, this material exhibits good redox reversibility under the condition of multiple reduction and re-oxidation cycles, as confirmed by the thermogravimetric analysis (TGA) measurements. A protonic fuel cell (PFC) built with this newly developed material shows a comparable electrocatalytic activity in both  $\text{C}_2\text{H}_6$  and  $\text{H}_2$  atmospheres while a considerably high power density of  $377 \text{ mW cm}^{-2}$  is achieved in  $\text{H}_2$  and  $268 \text{ mW cm}^{-2}$  in  $\text{C}_2\text{H}_6$  at 750 °C. In addition,  $\text{C}_2\text{H}_4$  yield in the cell with Co-SMCFO as anode is considerably improved (11.9%–37.8% at 650–750 °C) with respect to the widely used chromium oxide. The good electrochemical performance, the improved  $\text{C}_2\text{H}_6$  partial dehydrogenation ability and the negligible carbon formation in the Co-SMCFO anode are the strong indications that the SMCFO is a promising catalyst for the cogeneration of  $\text{C}_2\text{H}_4$  and electricity, and can also be potentially utilized in the PFC directly fueled with hydrocarbon.

## 1. Introduction

As one of the key reactions in the chemical industry,  $\text{C}_2\text{H}_6$  dehydrogenation to  $\text{C}_2\text{H}_4$  has been extensively studied in the past few decades due to the ever increasing demand for  $\text{C}_2\text{H}_4$ , a major intermediate for the production of polymers and petrochemicals [1,2]. Currently, the most widely employed technologies for  $\text{C}_2\text{H}_6$  dehydrogenation include 1) energy-intensive non-catalytic steam cracking at high temperature and 2) catalytic oxidative  $\text{C}_2\text{H}_6$  dehydrogenation. In comparison with the steam cracking, the oxidative dehydrogenation [a combination of endothermic reaction ( $\text{C}_2\text{H}_6$  dehydrogenation:  $\text{C}_2\text{H}_6 \rightarrow \text{C}_2\text{H}_4 + \text{H}_2$ ) and exothermic reaction ( $\text{H}_2$  oxidation:  $\text{H}_2 + 0.5 \text{O}_2 \rightarrow \text{H}_2\text{O}$ )] shows greater potential to lower the energy requirement and consequently improve the  $\text{C}_2\text{H}_4$  yield [3]. However, the presence of oxygen sources significantly consumes the produced  $\text{H}_2$  and causes undesirable deep oxidation of  $\text{C}_2\text{H}_6$  and/or  $\text{C}_2\text{H}_4$  to  $\text{CO}_2$  [4]. Therefore, developing alternative and more direct routes to dehydrogenate  $\text{C}_2\text{H}_6$  to  $\text{C}_2\text{H}_4$  is of particular interest. In this regard, protonic fuel cell (PFC) has emerged as a promising pathway to the solution of solving the problem [5,6]. In

a typical PFC utilized for cogenerating  $\text{C}_2\text{H}_4$  and electricity from  $\text{C}_2\text{H}_6$  oxidative dehydrogenation,  $\text{H}_2$  is selectively removed when the protons generated from the oxidation of  $\text{H}_2$  at anode pass through the protonic electrolyte and react with oxygen ions to form water at cathode. Moreover, since both  $\text{C}_2\text{H}_4$  and  $\text{C}_2\text{H}_6$  are prevented from contacting the oxygen sources, the  $\text{CO}_2$  emission resulted from deep oxidation can be avoided. Nonetheless, the minor oxide ion conductivity in the protonic electrolyte can significantly resist the carbon deposition at elevated temperatures [1,5].

Although conventional Ni-based materials show high catalytic activity towards fuel oxidation, they can be easily deactivated during cell operation due to their sensitivity to carbon formation as a result of incomplete hydrocarbon oxidation [7,8]. However, when perovskite is utilized as supporting backbone, the incorporated B-site cation in the perovskite lattice can be partially *in situ* exsolved as functional metal nanoparticle under reducing flow, which can not only serve as co-catalyst for certain reactions, but also improve the electronic conductivity of the parent perovskite [9–11]. More importantly, this exsolving process is able to grow much finer and more evenly distributed

\* Corresponding authors.

E-mail addresses: [xz.fu@szu.edu.cn](mailto:xz.fu@szu.edu.cn) (X.-Z. Fu), [jingli.luo@ualberta.ca](mailto:jingli.luo@ualberta.ca) (J.-L. Luo).

nanoparticles without agglomeration and carbon formation as compared to the deposited analogues [9]. Various perovskite oxides with *in situ* exsolved metal/bimetal nanoparticles, such as Ni-(La)Sr(Ni)TiO<sub>3</sub> [9], Ni-Sr<sub>2</sub>FeMo(Ni)O<sub>6</sub> [12], CoFe-La(Sr)(Co)FeO<sub>3</sub> [13] and CoFe-(Pr)Sr<sub>3</sub>[Fe(Nb)]<sub>2</sub>O<sub>7</sub> [14], have been investigated as potential anodes for solid oxide fuel cell (SOFC) using hydrocarbon gases. These anode materials show excellent catalytic activity and improved coking resistance towards hydrocarbon oxidation. One of the alternatives is the family of MMoO<sub>3</sub> (M = Sr, Ba, Ca) perovskites [15,16], especially the cubic SrMoO<sub>3</sub>; they have been demonstrated the high electrical conductivity ( $10^4 \text{ S cm}^{-1}$ ) at room temperature and high catalytic activity for oxidative dehydrogenation due to the presence of redox couple of Mo<sup>6+</sup>/Mo<sup>4+</sup> [16]. Furthermore, doping with trivalent elements (Co, Fe, Cr) of stoichiometric amounts at the Mo-sites potentially enhances the mixed ionic and electronic conductivity, as identified by the group of Martínez-Coronado [17–19]. Co is an excellent electrochemical catalyst with similar catalytic properties as Ni and has less tendency towards carbon formation, thus Co has been widely studied as an anode material in SOFC [20,21]. It has also been reported that group VIII metals are capable of catalyzing C<sub>2</sub>H<sub>6</sub> dehydrogenation with an activity sequence of Co > Ni > Fe [22]. Its good catalytic activity and high selectivity for C<sub>2</sub>H<sub>4</sub> make Co the most attractive-candidate for this reaction [23].

In this work, catalytically active Co metallic nanoparticles were successfully exsolved and evenly distributed on the porous cubic SrMo<sub>0.8</sub>Co<sub>0.1</sub>Fe<sub>0.1</sub>O<sub>3-δ</sub> (Co-SMCFO) framework to improve the C<sub>2</sub>H<sub>6</sub> dehydrogenation activity and electrochemical performance of the PFC by reducing SMCFO in 5% H<sub>2</sub>/N<sub>2</sub> flow at 850 °C. This material thus fabricated was used as anode in a BaCe<sub>0.7</sub>Zr<sub>0.1</sub>Y<sub>0.2</sub>O<sub>3-δ</sub> (BCZY) electrolyte-supported PFC. We systematically investigated the newly developed material in terms of its redox stability, the phase transformation, electrochemical performance, and C<sub>2</sub>H<sub>6</sub> dehydrogenation activity towards C<sub>2</sub>H<sub>4</sub> formation as well as the coking resistance. The mechanism credited for the good electrochemical performance and the high activity of C<sub>2</sub>H<sub>6</sub> oxidative dehydrogenation towards C<sub>2</sub>H<sub>4</sub> was also explored.

## 2. Experimental

### 2.1. Preparation and characterization of materials

Stoichiometric amounts of Sr(NO<sub>3</sub>)<sub>3</sub>, (NH<sub>4</sub>)<sub>6</sub>Mo<sub>7</sub>O<sub>24</sub>·4H<sub>2</sub>O, Co(NO<sub>3</sub>)<sub>2</sub>·6H<sub>2</sub>O and Fe(NO<sub>3</sub>)<sub>3</sub>·9H<sub>2</sub>O were dissolved in EDTA-NH<sub>3</sub>H<sub>2</sub>O solution under continuous heating and stirring, citric acid was then added. The molar ratio of EDTA acid: citric acid: total metal ions was controlled to be around 1: 1.5: 1. Subsequently, NH<sub>3</sub>H<sub>2</sub>O was added to adjust the pH value to be around 8. The solution was stirred and heated on a hot plate at 80 °C until the formation of organic resins containing the homogeneously distributed cations because of the slow evaporation of the solvent. The synthesized gel was decomposed at 300 °C for 4 h to remove the organic components and the nitrates. The precursor powders were then fired at 1100 °C for 10 h in air to obtain the raw materials which were subjected to further heating in a tubular furnace at 850 °C for additional 10 h in a reducing gas flow ( $\sim 10^{-19}$  atm of P<sub>O2</sub>) to eventually form the *in situ* exsolved Co-SMCFO.

Thermogravimetric analyses (TA SDT Q600) were performed from 20 to 1000 °C at a heating/cooling rate of 10 °C min<sup>-1</sup> in air or 5% H<sub>2</sub>/N<sub>2</sub> to characterize the thermophysical properties. The crystalline structure of all the synthesized powders was identified by X-ray diffraction (XRD) with Rigaku Rotaflex Cu Kα radiation (40 kV, 44 mA) and the raw data were analyzed with JADE version 6.5. Microstructures were determined with a high-resolution Zeiss Sigma FE-SEM equipped with an EDX detector and an EBSD detector. X-ray photoelectron spectroscopy (XPS, Kratos AXIS Ultra) was used to investigate the surface chemistry of the SMCFO and Co-SMCFO powders with the CasaXPS software, the adventitious carbon (C 1s) at the binding energy (BE) of 284.6 eV was used as the reference. Nicolet Almega XR Dispersive

Raman Microscope with 532 nm laser and X50 objective was used to determine the level of coke deposition on the Co-SMCFO after the stability test.

### 2.2. Cell fabrication and testing

The single cells investigated in this work were BCZY electrolyte supported. The anode material slurry was prepared by combining Co-SMCFO or NiO and BCZY (weight ratio of 1:1) with a glue containing 1-butanol, benzyl butyl phthalate (BBP), ethyl cellulose and alpha-terpineol. The weight ratio of catalyst and glue was 1.7:1. A cathode electrode comprised of LSCF and BCZY was prepared with the same method as that for the anode material slurry. Both the anode and cathode material slurries were screen-printed onto the corresponding surfaces of the BCZY disc to form a membrane electrode assembly (MEA). The MEA was sintered at 1000 °C for 2 h in air. Gold paste was painted onto the surfaces of both anode and cathode to form current collectors. The PFC was built by fixing the MEA between coaxial pairs of alumina tubes with a sealant, which was fastened in a vertical tubular furnace (Thermolyne F79300). Dry C<sub>2</sub>H<sub>6</sub> was fed to the PFC with a flow rate of 100 ml min<sup>-1</sup> via the anode tube located on the bottom, while the cathode, placed on the top, was exposed to air.

Electrochemical measurements were performed after the furnace reached a stable temperature. The electrochemical performances of the cell were measured by employing a four-probe method with Au wires as the leads. The electrochemical measurements were conducted with a Solartron 1255 frequency response analyzer and a Solartron 1286 electrochemical interface instrument. The temperature of a single cell was slowly increased to 850 °C and a 5% H<sub>2</sub>/N<sub>2</sub> reducing gas flow was continuously pumped into the anode compartment. The temperature was held for 2 h to complete the further reduction of the anode material, the temperature was then decreased to 750 °C and 700 °C for electrochemical measurements. Stability test in C<sub>2</sub>H<sub>6</sub> atmosphere was performed under a constant current load at 700 °C. The outlet gases from the anode compartment were analyzed using a Hewlett-Packard model HP5890 GC equipped with a packed bed column (Porapak QS) operated at 80 °C with a thermal conductivity detector and a flame ionization detector.

## 3. Results and discussion

The precursor powders of SMCFO were synthesized using a modified sol-gel method, as described elsewhere [24]. The corresponding X-ray diffraction (XRD) pattern of the SMCFO powders was obtained by Rigaku diffractometer (Cu Kα radiation, 40 kV, 44 mA) after firing in air at 1100 °C for 10 h (Fig. 1a). Clearly, the as-synthesized powders are a mixture of cubic (†) and tetragonal phases (Δ), where the standard SrCoO<sub>2.29</sub> (PDF #39-1083) shows a cubic structure with lattice constants of a = b = c = 3.912 Å, and the standard SrMoO<sub>4</sub> possesses a tetragonal phase [space group: 141/a(88)] with lattice parameters of a = b = 5.394 Å and c = 12.020 Å. However, it is found that SMCFO shows a pure single phase (PDF # 24-1224) without any impurities after firing in a reducing atmosphere (Fig. 1b). This agrees well with the standard structure of SrMoO<sub>3</sub> in the space group of pm-3 m (221) with the lattice constants of a = b = c = 3.974 Å, which indicates the successful preparation of SMCFO under reducing condition. The elimination of the SrCoO<sub>2.29</sub> is due to the Co exsolution and the annihilation of oxygen vacancies. Generally, the introduction of the cations with smaller ionic radius like Co<sup>3+</sup> (0.615 Å) and high spin Fe<sup>3+</sup> (0.645 Å) at B-site of Mo<sup>3+</sup> (0.65 Å) increases the 2θ and θ; angles and consequently, decreases the unit cell parameters [17,25,26]. A closer examination of the enlarged zone at the phase of (100) reveals that the diffraction peak of SMCFO after firing in reducing flow shifted to a larger angle as expected with corresponding diffraction angle changing from 22.38° to 22.55° (Fig. 1c). It is also worth mentioning that the substitution of B-sites by lower valence cations of Co and Fe causes the

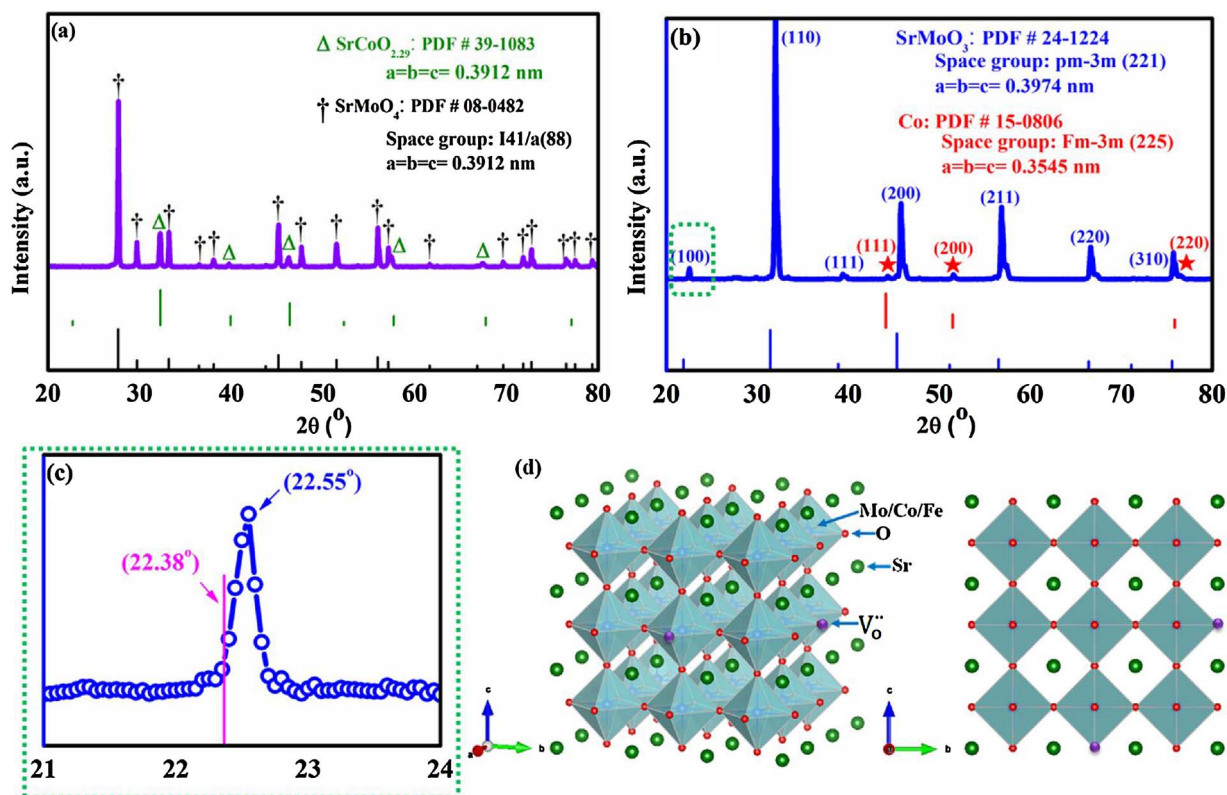


Fig. 1. X-ray diffraction patterns of SMCFO (a) before and (b) after sintering at 850 °C in 5% H<sub>2</sub>/N<sub>2</sub> atmosphere for 2 h; (c) enlarged zone at the phase of (100) in Fig. 1b; (d) the corresponding crystal structure.

formation of oxygen vacancies and/or interstitials to maintain the electroneutrality (see the crystal structure in Fig. 1d, the purple dot stands for the oxygen vacancy), which can account for the increased mixed electronic and ionic conductivity [27]. The peaks marked with “★” in Fig. 1b were assigned to the diffraction peaks of the *in situ* exsolved Co nanoparticles [PDF # 15-0806, space group: Fm-3m(225)] with lattice parameters of  $a = b = c = 3.545 \text{ \AA}$  from the SMCFO framework.

To further confirm the phase transformation of the as-synthesized SMCFO in reducing flow, TGA measurements were carried out in 5% H<sub>2</sub>/N<sub>2</sub> from 20 to 1000 °C. The weight loss of SMCFO in H<sub>2</sub> as a function of temperature is recorded in Fig. 2a; the inset shows the corresponding differential thermal analysis between 400 and 600 °C. The weight loss below 310 °C is probably due to the desorption of adsorbed water under ramping process [28]. Upon continuous heating, a sharp weight loss was observed between 400 and 600 °C, which is, in most part, attributed to the oxygen vacancy formation and/or the decrease of the oxygen content in the SMCFO. Apart from the XRD results, the occurrence of phase change was also detected by the differential thermal analysis as shown in the inset of Fig. 2a which clearly indicates the presence of an exothermic peak (★) at 481.2 °C. Such a phenomenon was also observed in the perovskite oxide of Pr<sub>0.5</sub>Ba<sub>0.5</sub>MnO<sub>3</sub>; its exothermic peak appeared at around 400 °C [7]. By further increasing the temperature, oxygen vacancies were continuously introduced until a limit was reached, where the perovskite lattice could no longer accommodate oxygen vacancies any more. At this point, continued reduction led to the *in situ* exsolution of B-site dopant and its simultaneous transformation to metal nanoparticles [29]. To evaluate the accurate content change of oxygen vacancy in reducing flow and its subsequent re-oxidation in air, the TGA measurement was immediately conducted in air for those reduced powders in H<sub>2</sub> under the same experimental conditions (Fig. 2b). It was found that a significant weight gain occurred in air during the heating process, which is attributed to the re-oxidation of the Co-SMCFO back to SMCFO and is

indicative of an increase in oxygen content. The weight changes of 4.68 wt% and 4.96 wt% were obtained in reducing flow and air flow, corresponding to the oxygen loss and uptake, respectively. On the basis of Wagner's theory [30], the magnitude of the calculated non-stoichiometry  $\delta$  for SMCFO in reducing flow is 0.654 at 1000 °C, which is quite close to the value ( $\delta = 0.693$ ) for Co-SMCFO in air. The well-matched results from the cyclic reduction and re-oxidation measurements demonstrate an excellent redox stability of the as-synthesized SMCFO. For the purpose of further confirming the calculated values of  $\delta$  based on the TGA results, XPS analysis was carried out to investigate the surface elements as well as the lattice oxygen and adsorbed oxygen before and after the reduction, as shown in Figs. 2c and d. The binding energy (BE) of 284.6 eV corresponds to the C1s, which was employed as a reference for all calibrations. The XPS survey spectra in Fig. 2c confirms the presence of Sr, Mo, Co and Fe in the SMCFO and Co-SMCFO powders. In general, the lattice oxygen on the surface of as-synthesized powders shows a peak at a BE of ~528 eV while the adsorbed oxygen at ~531 eV, the latter is related to the surface oxygen vacancies [31]. Fig. 2d shows the splitting peaks of O 1s for the powders before and after reduction. As can be seen, a significant increase in the adsorbed oxygen was observed on the surface of the reduced sample (Fig. 2d2) as compared to the one before the reduction (Fig. 2d1). This in turn confirms the formation of oxygen vacancies and the subsequent *in situ* exsolution of Co nanoparticles in the reducing flow. The corresponding O 1s quantitative analyses of the surface oxygen vacancies and the lattice oxygen are summarized in Table 1. The difference in adsorbed oxygen (oxygen vacancy) for both SMCFO and Co-SMCFO is 0.505.

In order to confirm the exsolution of Co nanoparticles more intuitively, scanning electron microscopy (SEM) along with energy-dispersive spectroscopy (EDS) was used to conduct analyses on both samples before and after reduction. The microstructures of the as-prepared SMCFO and reduced perovskite Co-SMCFO are displayed in Figs. 3a and b, respectively. As can be seen, the as-prepared SMCFO shows porous and well-interconnected structure with a glossy particle



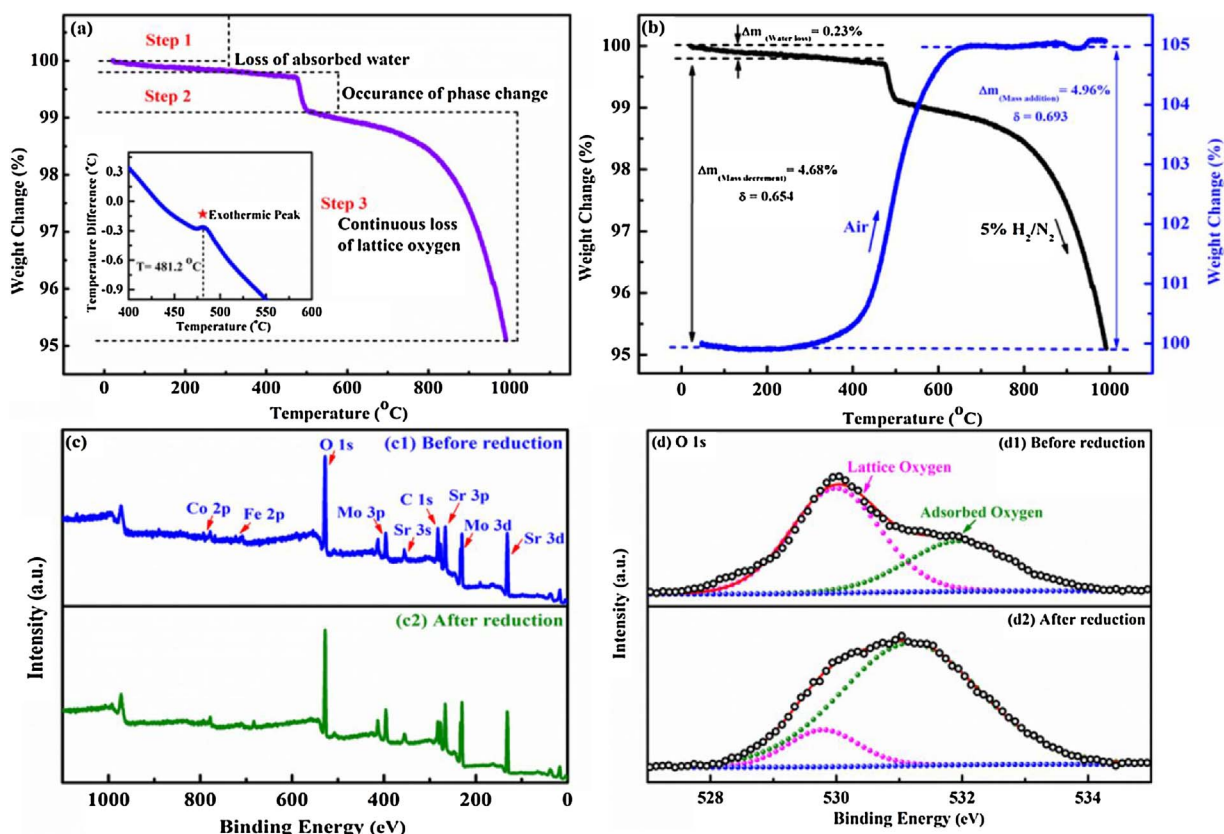


Fig. 2. Thermogravimetric analyses testing. (a) Weight loss and differential thermal analyses of SMCFO powders in reducing atmosphere, and (b) redox cycling ability test of SMCFO powders in 5% H<sub>2</sub>/N<sub>2</sub> and air flow at the same temperature range; (c) representative XPS survey spectra of all elements, and (d) O 1s spectra.

Table 1

Quantitative analysis of lattice oxygen and adsorbed oxygen on the surface of SMCFO and Co-SMCFO.

Catalyst	Area of lattice oxygen	Area of adsorbed oxygen
SMCFO	2818.5 (64.294%)	1565.5 (35.706%)
Co-SMCFO	457.5 (13.407%)	2955.2 (86.593%)

surface, an indication of fast gas diffusion ability and high mechanical strength. After firing in reducing flow at 850 °C for 2 h, the morphology of the reduced perovskite (Fig. 3b) is apparently different from the one obtained in air. Many nanoparticles were *in situ* exsolved and well-distributed on the surface of SMCFO backbone with an average diameter of 50 nm. In light of the XRD results, those exsolved, nano-sized particles are identified to be Co by the EDS spectrum and EDS elemental mappings shown in Figs. 3c and d, respectively. The EDS spectrum in Fig. 3c confirms the presence of Sr, Mo, Co and Fe in the Co-SMCFO. The position of the selected nanoparticle shows stronger signal, corresponding to the element Co (pink). In contrast, the much weaker and negligible signals are associated with the elements Sr (olive), Mo (magenta) and Fe (purple), indicating that only Co was *in situ* exsolved in the form of nanoparticles from the SMCFO backbone in reducing flow. Therefore, it is concluded that firing SMCFO in H<sub>2</sub> can consequently lead to the occurrence of a phase transformation (from mixed to pure structure) and subsequent *in situ* exsolving process of Co nanoparticles on the surface of the SMCFO backbone at elevated temperature. Moreover, the high oxygen vacancy content, derived from the phase transformation and the reduction of cations to lower oxidation states in the reduced perovskite, is beneficial for electrical conduction and catalytic activity towards the oxidation of fuels [7,12,14]. This makes Co-SMCFO a promising anode material to be utilized in PFC for the oxidation of hydrocarbons.

To evaluate the electrochemical performance of the PFC with the synthesized Co-SMCFO, an anode composite (BCZY and Co-SMCFO in a weight ratio of 1:1) was fabricated in a BCZY electrolyte-supported cell with cathode composite of (La<sub>0.6</sub>Sr<sub>0.4</sub>)<sub>0.95</sub>Co<sub>0.2</sub>Fe<sub>0.8</sub>O<sub>3</sub> and BCZY in a weight ratio of 1:1. Dry C<sub>2</sub>H<sub>6</sub> passed through the anode chamber continuously at a rate of 100 ml min<sup>-1</sup>, and the cathode was exposed to the air. After initiation stage, C<sub>2</sub>H<sub>6</sub> was partially dehydrogenated to C<sub>2</sub>H<sub>4</sub> and H<sub>2</sub>, the latter was then oxidized to protons at anode side and the protons subsequently reacted with oxygen ions at cathode. Obviously, if the protons are continuously removed, the C<sub>2</sub>H<sub>6</sub> oxidative dehydrogenation will not be limited by the thermodynamic equilibrium. The temperature-dependent potential and power density plots as a function of current densities in C<sub>2</sub>H<sub>6</sub> are recorded in Fig. 4a. As displayed, the open-circuit voltages (OCV) at the elevated temperatures are quite close to the thermodynamic reversible potentials, indicative of the good sealing state of the working cell. The PFC with Co-SMCFO in C<sub>2</sub>H<sub>6</sub> reached maximum power densities of 219 and 268 mW cm<sup>-2</sup> at 700 and 750 °C, respectively. The achieved maximum power densities are considerably higher than those of the recently reported materials, such as platinum paste (151 mW cm<sup>-2</sup> at 700 °C) [32], platinum paste in an anode-supported cell (216 mW cm<sup>-2</sup> at 700 °C) [33] and chromium oxide (118 mW cm<sup>-2</sup> at 750 °C) [34]. Moreover, Co-SMCFO shows a higher power density as compared with the SMCFO at 700 °C (Fig. 4a). This demonstrates the excellence of Co-SMCFO as an electrochemically active anode catalyst for direct C<sub>2</sub>H<sub>6</sub> fueled PFC. In addition, the electrocatalytic activity of the Co-SMCFO anode towards dry H<sub>2</sub> was also evaluated. The maximum power density of the PFC is much higher in H<sub>2</sub> (377 mW cm<sup>-2</sup>) than that (268 mW cm<sup>-2</sup>) in C<sub>2</sub>H<sub>6</sub> at the same temperature (Fig. 4b). The enhanced electrochemical performance of Co-SMCFO is mainly attributed to the high electrocatalytic activity of the *in situ* exsolved Co nanoparticles towards H<sub>2</sub> oxidation. The Co nanoparticles embedded on the surface of the backbone can effectively

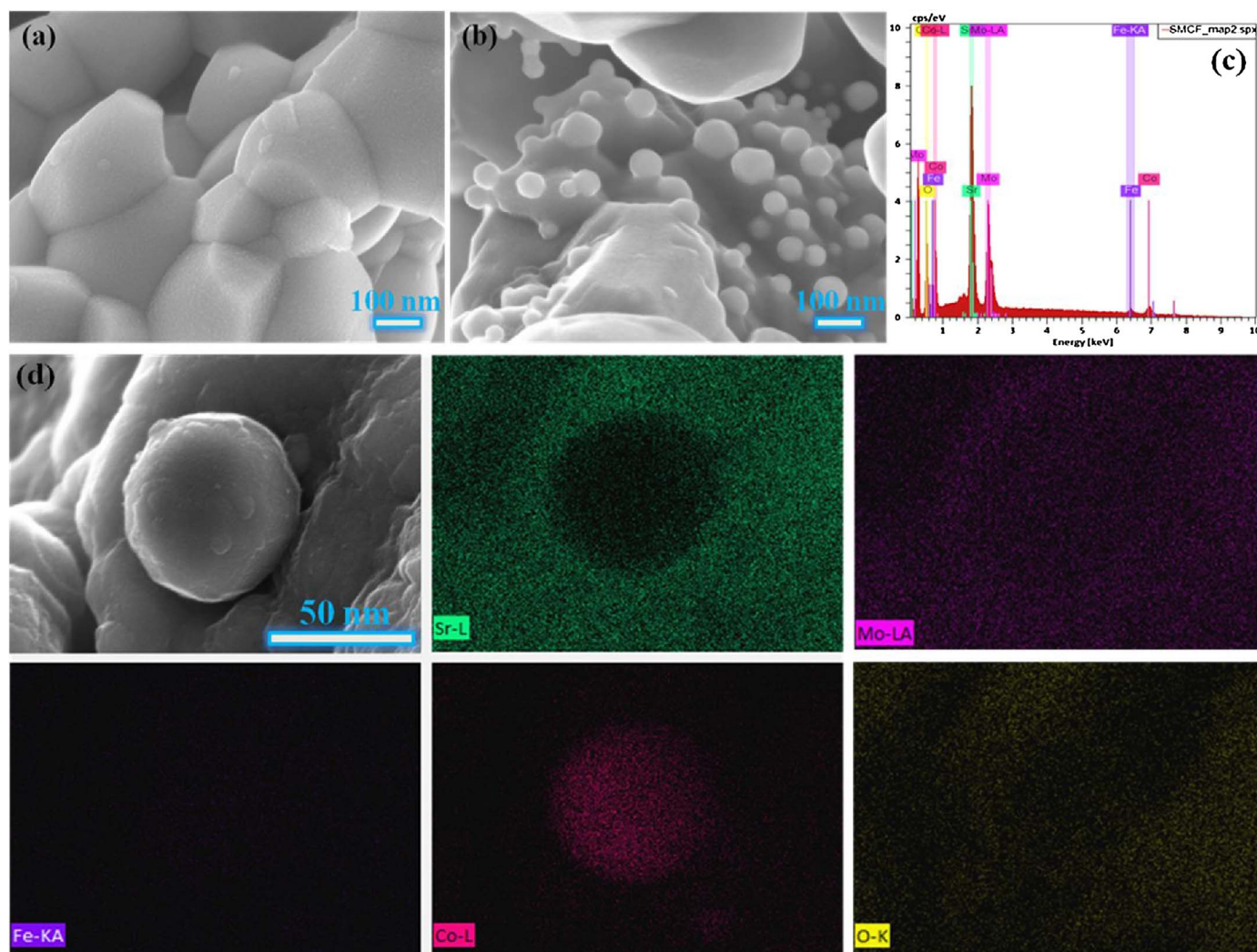


Fig. 3. SEM images of SMCFO powders (a) before and (b) after reduction in 5%  $H_2/N_2$  at 850 °C for 2 h; (c) EDS spectrum of Co-SMCFO and (d) the corresponding elemental mappings (Sr, Mo, Co, Fe and O).

promote the electrode reaction kinetics. Nevertheless, the slower electrode kinetics in  $C_2H_6$  is probably because of a newly identified low-frequency gas conversion process which is possibly related to the coupling of shift reaction and gas phase transport within the anode substrate [5,35,36]. Barnett's group also observed such phenomenon and concluded that only  $H_2$ , not other fuels, is directly and electrochemically oxidized within the anode functional layer [37], which consequently contributes to the lower overall polarization and higher power density for  $H_2$ . Above results have demonstrated that *in situ* exsolution of electrochemically active metallic nanoparticles from perovskite framework in reducing flow proves to be an effective way to boost the electrochemical performance of assembled cells. In evaluation of the dehydrogenation ability of Co-SMCFO in the PFC under applied peak current load, the outlet gases collected from the anode chamber were analyzed by online Gas Chromatography. The changes of  $C_2H_6$  conversions,  $C_2H_4$  selectivities and yields of Co-SMCFO and SMCFO under different conditions are presented in Fig. S2: the  $C_2H_6$  conversion of Co-SMCFO@ peak current load considerably increased from 12.5% to 41.3% with rising the temperatures (Fig. S2a), the corresponding  $C_2H_4$  yield reached 26.5% at 700 °C and 37.8% at 750 °C, respectively, and the  $C_2H_4$  selectivity was over 91% at the elevated temperatures. The  $C_2H_4$  yield in the cell with Co-SMCFO was improved (11.9%–37.8% at 650–750 °C) as compared to that with the nanosized chromium oxide (8.3%–31.1% at 650–750 °C) [34], a widely studied catalyst due to its

outstanding catalytic activity for alkane dehydrogenation [38,39]. During the testing period, the main detectable byproducts were methane and carbon monoxide due to the trace amount of oxide ionic conductivity in the protonic electrolyte, especially when the temperature was over 700 °C [40,41]. This demonstrates that the proposed fuel cell design can largely avoid those issues encountered during tube furnace cracking. Based on Fig. 4(c), the Co-SMCFO@ peak current load shows higher  $C_2H_4$  yields as compared to the SMCFO@ peak current load at different temperatures. This clearly indicates that the exsolved Co nanoparticles are also beneficial in terms of improving the dehydrogenation performance. Apart from the promotional effect of the *in situ* exsolved Co nanoparticles, the increased catalytic activity for  $C_2H_6$  dehydrogenation most probably originates from the coexistence of the redox couple of  $Mo^{6+}/Mo^{4+}$  since  $MMoO_3$  ( $M = Sr$  and  $Ba$ ) has been demonstrated to be catalytically active for oxidative dehydrogenation of isopropanol to acetone [16]. This was confirmed by the XPS analysis of  $Mo_{3d}$  shown in Fig. 4d, where an increase occurred in the lower oxidation state of Mo, which directly resulted in an increased coexistence of  $Mo^{6+}/Mo^{4+}$ . Furthermore, the short-term stability of the cell with Co-SMCFO in  $C_2H_6$  was also investigated; the corresponding potential response versus time was recorded at a constant current density load of  $0.39 A cm^{-2}$  at 700 °C (Fig. 5a). The potential stabilized at  $\sim 0.55 V$  for over 50 h, suggesting a negligible degradation during the testing period. After the stability test in  $C_2H_6$ , the cross-sectional



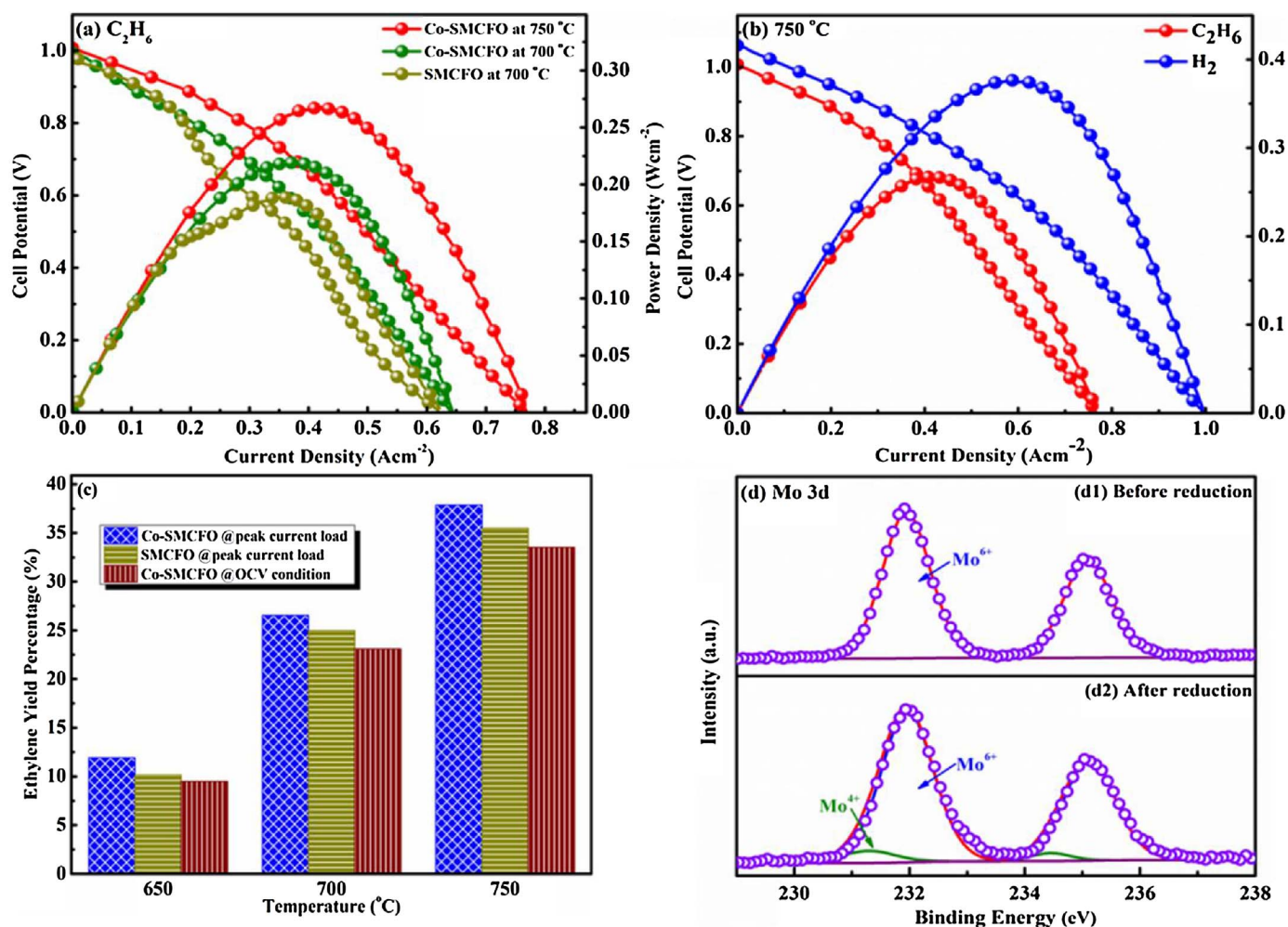


Fig. 4. Electrochemical performances of the PFC with Co-SMCFO anode material. (a) Current-voltage curves and corresponding power densities of the cell in  $C_2H_6$  at 700 °C and 750 °C; (b) current-voltage curves and corresponding power densities of the cell in  $C_2H_6$  and  $H_2$  atmospheres at 750 °C; (c)  $C_2H_4$  yields of SMCFO and Co-SMCFO as a function of temperature at different conditions; (d) XPS spectra of Mo 3d.

microstructure of the porous Co-SMCFO anode was examined (Figs. 5b and c). No delamination was detected (Fig. 5b) and the *in situ* exsolved Co nanoparticles were still embedded on the surface of the SMCFO framework without agglomeration (Fig. 5c). Besides, no visible carbon and carbon fibers were detected on the gas diffusion pathway of the anode. This is further confirmed by the *ex situ* Raman spectroscopy, see Fig. 5d, where there are no carbon featured peaks at 1338 (D band) and  $1568\text{ cm}^{-1}$  (G band) for the Co-SMCFO anode. In contrast, there are two strong peaks built up for the cell with Ni-based anode and the good coking resistance of the Co-SMCFO electrode for  $C_2H_6$  dehydrogenation is evident. In fact, Co catalyst is known to easily suffer from carbon deposition with carbon [42,43], however, the *in situ* exsolved Co nanoparticles can maintain crystallographic coherence with the backbone framework [9,44]. Additionally, the strong adhesion force between the backbone framework and the *in situ* exsolved Co nanoparticles can prevent carbon growth and the subsequent uplifting and agglomeration of Co nanoparticles.

#### 4. Conclusions

In summary, perovskite of SMCFO with *in situ* exsolved Co nanoparticles was synthesized by annealing the precursors prepared via modified sol-gel method in a 5%  $H_2/N_2$  reducing flow at 850 °C. The occurrence of phase change from a mixture of cubic and tetragonal structures to pure cubic structure in conjunction with the *in situ* exsolution of Co nanoparticles in reducing flow introduced certain

amount of oxygen vacancies ( $\delta = 0.654$ ), which account for the improved electrical conductivity and electrocatalytic activity towards the oxidation of fuels. A protonic fuel cell fabricated with this material exhibited excellent electrochemical performance and the cell reached the maximum power densities of  $377\text{ mW cm}^{-2}$  in  $H_2$  and  $268\text{ mW cm}^{-2}$  in  $C_2H_6$  at 750 °C, respectively. The corresponding  $C_2H_4$  yield of the cell with Co-SMCFO@ peak current load is 37.8% with the  $C_2H_4$  selectivity exceeding 91%, considerably higher than that with the commonly and widely used chromium oxide (31.1%) at the same temperature. Moreover, the cell with this newly developed material stabilized at a potential of 0.55 V under a constant current load at 700 °C for over 50 h, exhibiting an excellent coking resistance which was further confirmed by Raman spectroscopy. Combining its merits of the good redox reversibility under reduction and re-oxidation cycles, the excellent electrochemical performance, the improved  $C_2H_6$  partial dehydrogenation ability and negligible coking, the newly developed Co-SMCFO presents the strong potential to be directly utilized in PFC with hydrocarbon as the fuel.

#### Acknowledgements

This work was supported by the Natural Sciences and Engineering Research Council of Canada and National Natural Science Foundation of China (No.21203236).

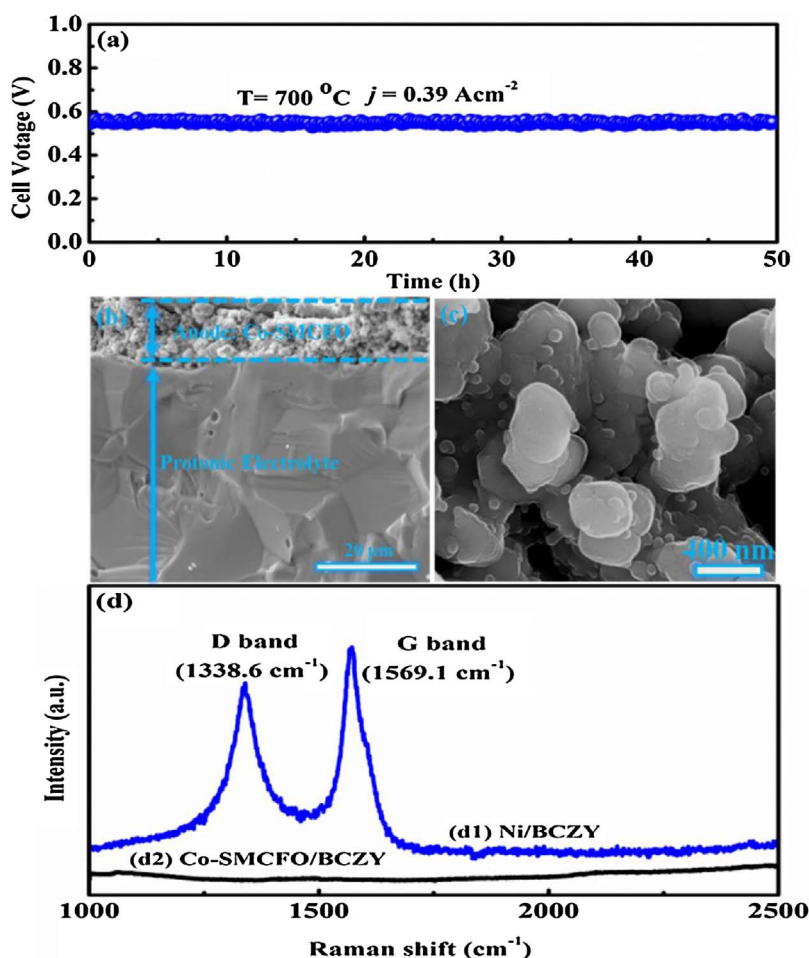


Fig. 5. (a) Short-term stability of the cell with Co-SMCFO under a constant current load of  $0.39 \text{ A cm}^{-2}$  at  $700^\circ\text{C}$ ; (b) SEM image of the anode and electrolyte cross section and (c) SEM image of anode after stability test; (d) Raman spectra collected from (d1) the Ni/BCZY anode surface and (d2) Co-SMCFO/BCZY anode surface after stability tests.

## Appendix A. Supplementary data

Supplementary data associated with this article can be found, in the online version, at <http://dx.doi.org/10.1016/j.apcatb.2017.08.051>.

## References

- H.H. Shin, S. McIntosh, *ACS Catal.* 5 (2015) 95–103.
- O.O. James, S. Mandal, N. Alele, B. Chowdhury, S. Maity, *Fuel Process. Technol.* 149 (2016) 239–255.
- M. Bhasin, J. McCain, B. Vora, T. Imai, P. Pujado, *Appl. Catal. A-Gen.* 221 (2001) 397–419.
- J.-L. Luo, X.Z. Fu, N. Danilovic, K.T. Chuang, A.R. Sanger, A. Krzywicki, United States patent US 8, 574, 786.
- S. Liu, K.T. Chuang, J.-L. Luo, *ACS Catal.* 6 (2015) 760–768.
- S. Liu, Y. Behnamian, K.T. Chuang, Q. Liu, J.-L. Luo, *J. Power Sources* 298 (2015) 23–29.
- S. Sengodan, S. Choi, A. Jun, T.H. Shin, Y.W. Ju, H.Y. Jeong, J. Shin, J.T. Irvine, G. Kim, *Nat. Mater.* 14 (2015) 205–209.
- M. Liu, M.E. Lynch, K. Blinn, F.M. Alamgir, Y. Choi, *Mater. Today* 14 (2011) 534–546.
- D. Neagu, T.S. Oh, D.N. Miller, H. Menard, S.M. Bukhari, S.R. Gamble, R.J. Gorte, J.M. Vohs, J.T. Irvine, *Nat. Commun.* 6 (2015) 8120.
- D. Neagu, G. Tsekouras, D.N. Miller, H. Menard, J.T. Irvine, *Nat. Chem.* 5 (2013) 916–923.
- B.D. Madsen, W. Kobsiriphat, Y. Wang, L.D. Marks, S.A. Barnett, *J. Power Sources* 166 (2007) 64–67.
- Z. Du, H. Zhao, S. Yi, Q. Xia, Y. Gong, Y. Zhang, X. Cheng, Y. Li, L. Gu, K. Swierczek, *ACS Nano* (2016).
- H. Chang, H. Chen, Z. Shao, J. Shi, J. Bai, S.-D. Li, *J. Mater. Chem. A* (2016).
- C. Yang, J. Li, Y. Lin, J. Liu, F. Chen, M. Liu, *Nano Energy* 11 (2015) 704–710.
- S. Hayashi, R. Aoki, T. Nakamura, *Mater. Res. Bull.* 14 (1979) 409–413.
- J. Kubo, W. Ueda, *Mater. Res. Bull.* 44 (2009) 906–912.
- R. Martínez-Coronado, J.A. Alonso, M.T. Fernández-Díaz, *J. Power Sources* 258 (2014) 76–82.
- R. Martínez-Coronado, J.A. Alonso, A. Aguadero, M.T. Fernández-Díaz, *Int. J. Hydrogen Energy* 39 (2014) 4067–4073.
- R. Martínez-Coronado, A. Aguadero, J.A. Alonso, M.T. Fernández-Díaz, *Mater. Res. Bull.* 47 (2012) 2148–2153.
- J. Zhou, T.-H. Shin, C. Ni, G. Chen, K. Wu, Y. Cheng, J.T.S. Irvine, *Chem. Mater.* 28 (2016) 2981–2993.
- Y.-F. Sun, Y.-Q. Zhang, J. Chen, J.-H. Li, Y.-T. Zhu, Y.-M. Zeng, B.S. Amirkhiz, J. Li, B. Hua, J.-L. Luo, *Nano Lett.* 16 (2016) 5303–5309.
- Y. Schuurman, V. Ducarme, T. Chen, W. Li, C. Mirodatos, G.A. Martin, *Appl. Catal. A-Gen.* 163 (1997) 227–235.
- R. Koirala, R. Buechel, S.E. Pratsinis, A. Baiker, *Appl. Catal. A-Gen.* 527 (2016) 96–108.
- C. Duan, J. Tong, M. Shang, S. Nikodemski, M. Sanders, S. Ricote, A. Almansoori, R. O'Hayre, *Science* 349 (2015) 1321–1326.
- R. Martínez-Coronado, J.A. Alonso, M.T. Fernández-Díaz, *J. Alloy Compd.* 607 (2014) 280–284.
- R. Martínez-Coronado, J.A. Alonso, A. Aguadero, M.T. Fernández-Díaz, *J. Power Sources* 208 (2012) 153–158.
- T. Ishihara, *Springer Sci. Bus. Media* (2009).
- D.J. Cumming, V.V. Kharton, A.A. Yaremchenko, A.V. Kovalevsky, J.A. Kilner, *J. Am. Ceram. Soc.* 94 (2011) 2993–3000.
- G. Tsekouras, D. Neagu, J.T.S. Irvine, *Energy Environ. Sci.* 6 (2013) 256–266.
- J. Mizusaki, Y. Mima, S. Yamauchi, K. Fueki, H. Tagawa, *J. Solid State Chem.* 80 (1989) 102–111.
- J.-W. Yin, Y.-M. Yin, J. Lu, C. Zhang, N.Q. Minh, Z.-F. Ma, *J. Phys. Chem. C* 118 (2014) 13357–13368.
- X.-Z. Fu, J.-L. Luo, A.R. Sanger, N. Luo, K.T. Chuang, *J. Power Sources* 195 (2010) 2659–2663.
- X.-Z. Fu, J.-L. Luo, A.R. Sanger, Z.-R. Xu, K.T. Chuang, *Electrochim. Acta* 55 (2010) 1145–1149.
- X.-Z. Fu, X.-X. Luo, J.-L. Luo, K.T. Chuang, A.R. Sanger, A. Krzywicki, *J. Power Sources* 196 (2011) 1036–1041.
- A. Kromp, A. Leonide, A. Weber, E. Ivers-Tiffée, *J. Electrochem. Soc.* 158 (2011) B980–B986.
- S. Wang, J.-L. Luo, A.R. Sanger, K.T. Chuang, *J. Phys. Chem. C* 111 (2007) 5069–5074.
- Y. Lin, Z. Zhan, J. Liu, S.A. Barnett, *Solid State Ionics* 176 (2005) 1827–1835.
- B.M. Weckhuysen, R.A. Schoonheydt, *Catal. Today* 51 (1999) 223–232.
- B.M. Weckhuysen, I.E. Wachs, R.A. Schoonheydt, *Chem. Rev.* 96 (1996) 3327–3350.
- S. Ricote, N. Bonanos, M.M. De Lucas, G. Caboche, *J. Power Sources* 193 (2009) 189–193.
- W. Suksamai, I. Metcalfe, *Solid State Ionics* 178 (2007) 627–634.
- K. Takanabe, K. Nagaoka, K. Nariai, K. Aika, *J. Catal.* 232 (2005) 268–275.
- K. Takanabe, K. Nagaoka, K. Nariai, K. Aika, *J. Catal.* 230 (2005) 75–85.
- S. Liu, Q. Liu, J.-L. Luo, *ACS Catal.* 6 (2016) 6219–6228.